Letter

Elastocapillary menisci mediate interaction of neighboring structures at the surface of a compliant solid

Lebo Molefe and John M. Kolinski [*]

Institute of Mechanical Engineering (IGM), School of Engineering (STI), Ecole Polytechnique Fédérale de Lausanne (EPFL), 1015 Lausanne, Switzerland

Surface stress drives long-range elastocapillary interactions at the surface of compliant solids, where it has been observed to mediate interparticle interactions and to alter transport of liquid drops. We show that such an elastocapillary interaction arises between neighboring structures that are simply protrusions of the compliant solid. For compliant micropillars arranged in a square lattice with spacing p less than an interaction distance p^*, the distance of a pillar to its neighbors determines how much it deforms due to surface stress: Pillars that are close together tend to be rounder and flatter than those that are far apart. The interaction is mediated by the formation of an elastocapillary meniscus at the base of each pillar, which sets the interaction distance and causes neighboring structures to deform more than those that are relatively isolated. Neighboring pillars also displace toward each other to form clusters, leading to the emergence of pattern formation and ordered domains.

Surface stress can completely change the shape of the interface of a compliant solid at sufficiently small scales [1–23], just as it leads to large deformation of small fluid volumes [24,25]. The excess tangential stress in a liquid-air interface promotes the instability of a cylindrical liquid jet, causing it to break into droplets [24] and surface stress has been observed to cause an analogous instability for cylinders of compliant solid gels [1]. Compliant solids routinely undergo large deformation in response to stresses that they are exposed to. However, the consequences for an interfacial structure that deforms subject to surface stress remain poorly understood.

The typical scale at which elastocapillary phenomena are expected to be observed is defined by the ratio of the surface stress Υ to the material's shear modulus G and is called the elastocapillary length $\ell_{\mathrm{ec}} = \Upsilon/G$ [26]; this arises from a comparison of capillary pressure to the strain in the bulk [2,3]. For structures at a solid-fluid interface with radius of curvature $\mathcal{R}$ below ℓ_{ec}, surface stress prompts rounding and large deformations [2,4]. In this way, regions of a surface that have initially small radius of curvature, such as the corners of a sharp feature, deform into regions of large radius of curvature that extend farther from the original feature and are in some cases reminiscent of liquid menisci. It is unknown how the deformation of a single structure influences the deformation of other structures at the interface and ultimately the entire interface geometry.

Here we probe the mutual interaction of deforming structures at the interface of compliant gels by molding grids of three-dimensional (3D) cuboid micropillar features with size similar to the material's elastocapillary length and varying the center-to-center spacing p between the microtextures.

Following release from the mold, the solid-air interface deforms due to surface stress. We experimentally study the deformed micropillar surface profiles through two metrics: their final deformed height h_d and mean curvature H. An elastocapillary interaction emerges below an interaction distance p^*. At distances $p < p^*$, pillar deformation is strongly dependent on the location of neighboring pillars.

The spacing-dependent pillar deformation generates two regimes of the system's behavior: Above the interaction distance p^*, a pillar's deformation depends only on its initial shape and material properties (ℓ_{ec}). Below p^*, however, proximity to neighboring structures increases deformation. The interaction is shown to be mediated by elastocapillary menisci formed at the base of each pillar. Within the elastocapillary interaction regime, besides the increase of individual pillar deformation, additional behaviors such as clustering emerge. In addition to its relevance for practical applications in microfabrication and other areas [5], our study also improves our fundamental understanding of surface stress, including highlighting the emergence of ordered domains.

Crucially, pillar interaction and clustering emerge in this system as a direct consequence of the pillars' aspect ratio, where their height h_0 is of a similar scale to their width w_0 (Fig. 1). Interaction between pillars is only observable due to large deformation of the pillar and the bulk material, which does not occur when $h_0/w_0 \ll 1$ [5–9].

Textured compliant surfaces are typically cast in a mold and separated by peeling once cured [5–9,27–29]. While this works well for low-aspect-ratio textures ($h_0/w_0 \ll 1$), it is ineffective for large-aspect-ratio textures where $h_0 \sim w_0$, because the compliant ($G \lesssim 1$ kPa) and highly adhesive material becomes stuck within the deep channels in the mold. During peeling, the material fails, destroying the surface textures. Thus, we developed a microfabrication technique based on dissolution where we cast a compliant silicone gel (PDMS
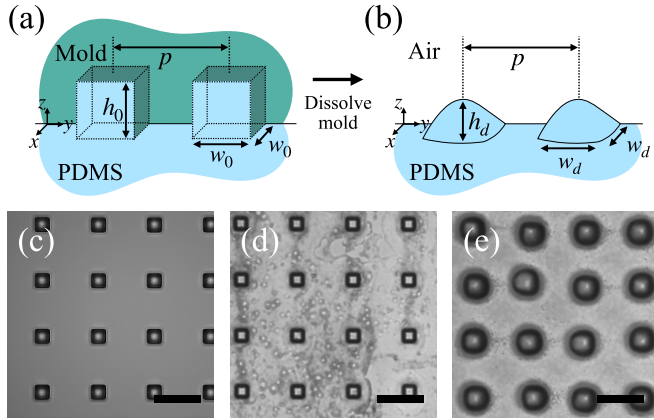
* john.kolinski@epfl.ch

FIG. 1. Surface fabrication using a dissolvable mold. (a) The mold shape is a grid of recessed rectangular prisms with center-to-center spacing p. (b) After dissolving the mold, the PDMS deforms to height h_d and width w_d. [(c)–(e)] Optical microcoscopy images for $p = 90$ μm of the (c) dissolvable mold; (d) stiff surface, $G \approx 60$ kPa; and (e) compliant surface, $G \approx 1$ kPa. The mold is well replicated by the stiff PDMS, whereas compliant PDMS significantly deforms. Scale bars are 100 μm.

CY 52-276, Dow Europe GmbH) into a dissolvable mold [Figs. 1(a)–1(b)]. The method of using a dissolvable mold has previously been used to study surface stress deformation of millimeter-scale elastic rods using styrofoam molds dissolved in toluene [1,10] and we demonstrate that this idea can also be applied to produce micrometer-scale patterns.

Using photolithography techniques, a grid of cuboid holes is patterned into a polymer-based photoresist to form a rigid mold (see Appendix A). A schematic of the mold is shown in Fig. 1(a), where each hole has depth $h_0 = 26$ μm and width $w_0 = 30$ μm. The holes are arranged on a square lattice with spacing p varying between 45 and 480 μm. Figure 1(c) is an image of the mold for $p = 90$ μm. The initial mold dimensions were verified by optical microscopy (for w_0) and optical profilometry (for h_0). After spin-coating a compliant gel into the mold and curing the material by baking, the gel layer is bonded to a glass surface for support. The whole ensemble is then placed in an acetone bath, where the mold dissolves, but the cast gel is left intact [30]. After dissolution of the mold, we remove the surface from acetone, immerse the surface in deionized water to rinse off the acetone, and dry the PDMS by leaving it in air [31].

Pillar height h_0 is small compared to the bulk thickness, estimated to be 200 μm based on the spin-coating speed. To vary the material stiffness, we vary the ratio of part A to part B in PDMS CY 52-276, producing a compliant surface (1:1 A:B ratio) and a stiff surface (1:10 A:B ratio). A schematic of the released textures is shown in Fig. 1(b), where they deform to a final height h_d and width w_d. The height h_d is defined as the distance between the pillar's peak and the surrounding surface after deformation, where we note that the deformation involves both pillar material displacing into the bulk material region and bulk material surrounding the pillar moving upward in the $+z$ direction [6]. Thus, h_d characterizes the deformed height of the pillar relative to the deformed final surface position.
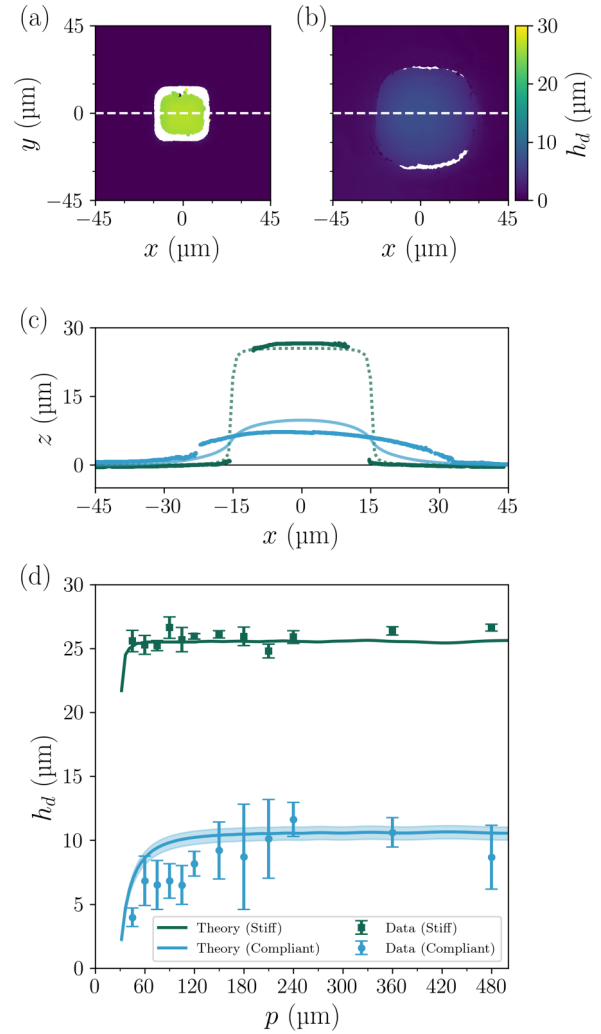

FIG. 2. Deformed surface profiles. (a) Height profile for a stiff micropillar, $G \approx 60$ kPa. (b) Height profile for a compliant micropillar, $G \approx 1$ kPa. Grid spacing in both cases is $p = 90$ μm. (c) Profiles of the stiff and compliant pillars as viewed along the dashed lines in (a) and (b). Data points are compared to a theoretical model for low-aspect-ratio features [11] in the stiff (dotted line) and compliant (solid line) cases. For the compliant pillar h_d is less than predicted. (d) Deformed height h_d of stiff pillars (squares) and compliant pillars (circles) as a function of grid spacing p. For compliant pillars, h_d decreases as p becomes small. The theory (solid lines) [11] is plotted with a shaded confidence band representing a 95% confidence interval in the shear modulus. The confidence band for the stiff material is too small to be visible.

To characterize the elastocapillary length, we measure the gel's shear modulus G with a rheometer (Anton Paar MCR 302). For the compliant material $G = 0.84 \pm 0.07$ kPa and for the stiff material $G = 63 \pm 2$ kPa. The surface stress is $\Upsilon = 35 \pm 5$ mN/m and was measured by imaging the wetting ridge of a glycerol drop deposited on the PDMS with a confocal fluorescence microscope (Leica SP8 STED 3X with a $93\times$ glycerol immersion lens, NA $= 1.3$). See Supplemental Material for material characterization details [32].

An interferometric profilometer (Bruker Contour X) is used to measure the solid-air interface profile. Figure 2

compares the deformed profiles of stiff [Fig. 2(a)] and compliant [Fig. 2(b)] micropillars at $p = 90 \ \mu$m. The stiff pillar has replicated the mold with fidelity, having the mold's original height $h_0 = 26 \ \mu$m, and also retaining the original lateral dimensions of the mold (30 μm × 30 μm), whereas the compliant one has become much shorter, rounding into an almost circular profile and expanding significantly in the xy plane. Figure 2(c) displays a side view of the profiles. We compare the profiles to the predicted deformation in a theory for 3D structures with low aspect ratio proposed by Hui *et al.* [11] and find that it models the stiff pillar well but overpredicts the height of the compliant one. This suggests that the theory may need modification for structures that have a characteristic scale similar to ℓ_{ec} but that do not satisfy the assumption of infinitesimal aspect ratio. Significant rounding and flattening of compliant pillars were similarly observed for all spacings $p = 45$–$480 \ \mu$m.

Figure 2(d) displays the deformed height h_d measured at the pillar center as a function of spacing p for surfaces of different stiffness. Error bars are 95% confidence intervals, where each data point represents the mean height of 30–146 pillars. The elastocapillary length of the stiff material is $\ell_{ec} \approx 0.5 \ \mu$m, so that we expect surface stress to have a minimal effect on structures at a 30 μm scale. Indeed, the stiff pillar heights match the original mold design ($h_0 = 26 \ \mu$m) across all spacings p. By contrast, the elastocapillary length of the compliant material is $\ell_{ec} \approx 42 \ \mu$m, so we expect surface stress to drive significant deformations. A compliant pillar's height h_d is highly dependent on spacing for low values of p, whereas h_d reaches a constant value as p increases [Fig. 2(d)]. We identify the length scale for the transition between these two behaviors around $p^* \approx 120$–$150 \ \mu$m, which defines the elastocapillary interaction distance. For $p < p^*$, a pillar's deformation is affected by its neighbors, whereas for $p > p^*$, deformation depends only on the pillar's initial shape and material properties G and Υ.

We observe a similar trend in the mean curvature H as a function of p [39]. We show in Appendix B that pillars deform into approximately spherical caps, with a well-defined curvature H_0 and radius of curvature $\mathcal{R} = 1/|H_0|$. Figure 3 displays $\mathcal{R}$ as a function of p for compliant pillars. Error bars have the same meaning as in Fig. 2(d). $\mathcal{R}$ is largest at small spacings, whereas it decreases to a constant value as p increases, indicating that close pillars flatten significantly more (having larger radius of curvature) than relatively isolated ones. Notably, the transition to a constant curvature occurs at the same distance $p^* \approx 120$–$150 \ \mu$m identified in the analysis of h_d [Fig. 2(d)].

The increased deformation and rounding for $p < p^*$ suggests an elastocapillary interaction between pillars. To probe this interaction, we measure the curvature field $H(x, y)$ around a relatively isolated pillar, as shown in Fig. 4(a). In Fig. 4(b), we observe that the curvature field has almost constant negative curvature near the top of the pillar, which becomes positive where the pillar meets the surface and subsequently decays to zero. By doing the same analysis for several pillars [Fig. 5(c)], we observe that the curvature consistently decays with a characteristic distance of $s^* \approx 60 \ \mu$m. This horizontal decay length defines the scale of an elastocapillary meniscus. The elastocapillary meniscus scale s^* is of the same order
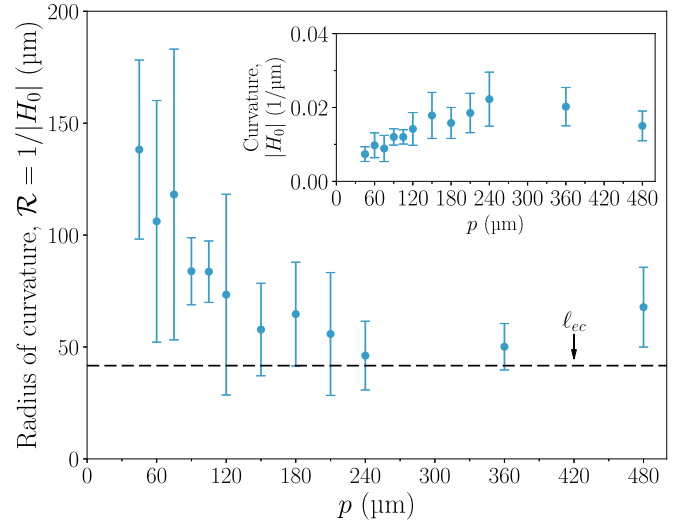

FIG. 3. Radius of curvature $\mathcal{R}$ as a function of p. Deformed curvature depends on spacing. As $p \to 0$, radius of curvature increases—in other words, pillars are flatter. Dashed line is the elastocapillary length ℓ_{ec}. (inset) Curvature $|H_0|$ as a function of p.

as the elastocapillary length ℓ_{ec}. Notably, the pillar shape that was originally square in the xy plane becomes nearly axisymmetric, as is evident in Fig. 4(a) and discussed in detail in Supplemental Material [32].

The scale of the curvature decay $s^* \approx 60 \ \mu$m is about half of the scale of the interaction distance $p^* \approx 120$–$150 \ \mu$m. This relation $s^* = p^*/2$ is a clear indication that the interaction between pillars is mediated by their elastocapillary menisci: For a pair of pillars, the length scale $2s^*$ is the scale at which the meniscus of one pillar touches that of another pillar—schematically illustrated in Fig. 5(a). This is the same length scale $p^* = 2s^*$ at which we observe spacing-dependent deformation. As the meniscus scale s^* is of the same order as ℓ_{ec}, we also observe $p^* \sim 2\ell_{ec}$, which relates the interaction distance p^* to the elastocapillary length ℓ_{ec}.

To illustrate more clearly what happens to the elastocapillary menisci in the valley between neighboring pillars as compared to isolated ones, in Fig. 5(b) we overlay profiles of two isolated pillars (gray) whose original spacing was $p = 360 \ \mu$m as if they were separated by a distance of $p = 60 \ \mu$m. The superposition of two relatively isolated pillars represents a hypothetical scenario where elastocapillary interaction with neighboring pillars does not affect deformation. The region where the menisci overlap near $x = 0 \ \mu$m in this hypothetical situation has a higher curvature than the tops of the pillars, and we observe that the profile of a real interface (orange) is rounder by comparison. Thus, as a result of rounding and lifting bulk material between pillars, as well as decreasing pillar height, the meniscus decreases the surface area and curvature, likely reducing the total energy of the system.

Elastocapillary interaction not only increases individual pillar deformation but also leads to displacement of pillar centroids, such that groups of pillars form clusters [Figs. 5(c) and 5(d)]. Clustering for a group of pillars can be quantified by the root-mean-squared deviation (RMSD) of pillar centroids from their ideal grid positions, divided by the initial space
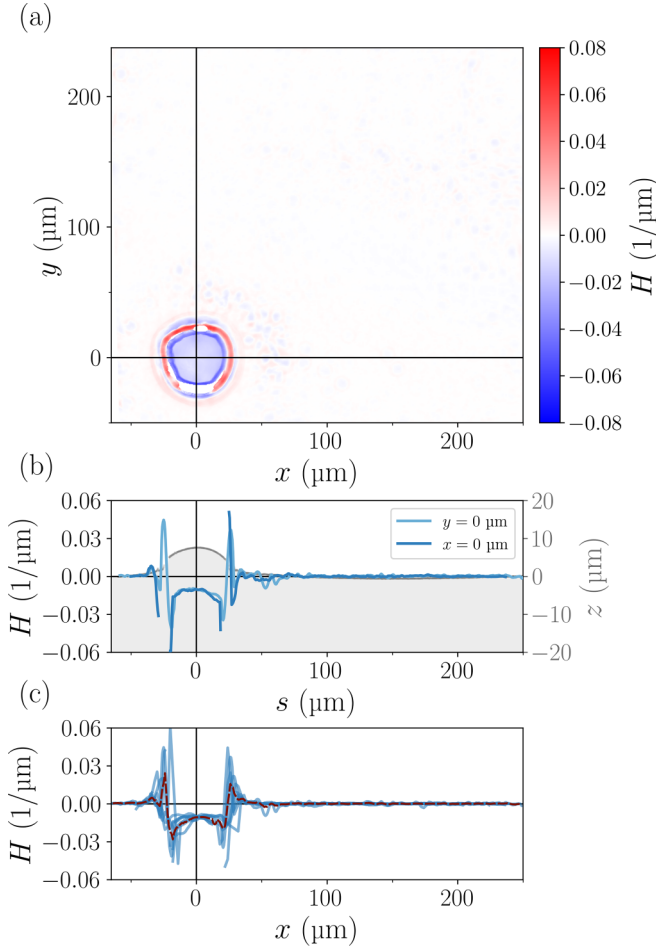
FIG. 4. Elastocapillary meniscus scale. (a) Mean curvature field $H(x, y)$ around a pillar with $p = 480$ μm. (b) H as a function of position s along $y = 0$ (light blue) and $x = 0$ (dark blue). The pillar profile is plotted in gray. (c) Curvature along $y = 0$ for eight different pillars with $p = 480$ μm. The red dashed line is a moving average using bin width of 3 μm. Beyond ~60 μm from the pillar center, curvature decays to zero.
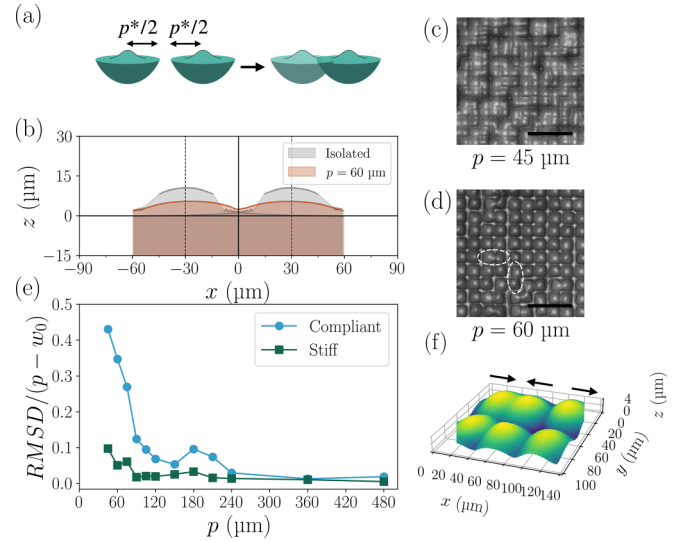

FIG. 5. Interaction of elastocapillary menisci. (a) Schematic of a pair of pillars depicting elastocapillary meniscus scale $s^* \approx p^*/2$. When the distance between adjacent pillars is below p^*, pillars interact. (b) Profile of adjacent pillars (orange) at spacing $p = 60$ μm. Gray profile is a pillar at large spacing ($p = 360$ μm) that is duplicated so we can visualize the hypothetical overlap of its elastocapillary meniscus with another isolated pillar. [(c) and (d)] Optical microscopy of compliant pillar clusters at (c) $p = 45$ μm and (d) $p = 60$ μm. Scale bars are 200 μm. (e) Clustering behavior, quantified by pillar centroids' root-mean-squared deviation (RMSD), divided by $(p - w_0)$. (f) Profilometry data depict arrested coalescence of a clustered pair for $p = 90$ μm.

$(p - w_0)$ between two pillar edges. If the deviation of a pillar and its neighbor toward each other is equal to half the distance between two pillar edges ($\frac{p - w_0}{2}$), then the pillars will touch. The RMSD of the ensemble of compliant pillars has a value such that RMSD/$(p - w_0) \approx 1/2$ for the lowest spacings $p = 45$–75 μm, indicating high levels of clustering that are not observed for the stiff material [Fig. 5(e)]. A single pair of pillars that have displaced toward each other is depicted in Fig. 5(f).

In this work, we demonstrate that neighboring structures at a solid-air interface can interact through an elastocapillary meniscus, leading to pronounced deformation and rounding. We introduce a microfabrication technique for producing structures at the surface of a compliant solid and study how their deformation to final height h_d and mean curvature H depends on grid spacing p. Deformation depends on spacing for $p < p^*$ where $p^* \approx 2s^*$ is set by the horizontal scale s^* of the elastocapillary meniscus around a deformed pillar. Excess deformation due to elastocapillary interaction is significant— the most closely spaced pillars shrink to around 20% of their

initial height, $h_d \approx 0.2h_0$. This is much less than the deformed height of a relatively isolated pillar, $h_d \approx 0.5h_0$.

In addition to large deformations, pillar centroids displace from their initial grid positions, similarly to droplet "durotaxis" or the attraction between glass beads at a gel-air interface, which are also mediated by regions of nonzero curvature between the objects [12–14]. Here we observe similar long-range elastocapillary interaction between structures that are part of the interface itself, without introducing external objects. This system is an attractive alternative for studying elastocapillary interaction at interfaces, because the singularity at the contact line is not present. Interaction between pillars also differs from the interactions between external objects, however: First, a pillar's displacement toward its neighbor is limited due to the elastic energy cost. Second, a pillar's final shape is affected by the interaction, which does not occur for objects such as rigid beads. Excess deformation and rounding are added mechanisms by which pillars decrease the surface area of their elastocapillary menisci. Intriguingly, we observe the emergence of pattern formation in a system driven solely by the solid's surface stress; by contrast, clustering patterns previously observed for stiff micropillar arrays are driven by liquid-air surface tension [40–45]. Our observations suggest future directions for introducing defects or varied initial conditions to better characterize emergence of order at low p.

Beyond the fundamental study of surface stress, our experiments suggest new directions toward probing self-assembly on gel and elastomer interfaces [12,13,46] by using
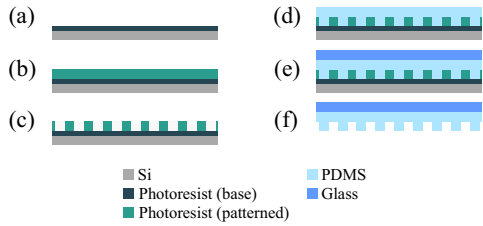
FIG. 6. Microfabrication procedure. A silicon wafer is coated with (a) a 2-μm layer of photoresist (AZnLOF2020, Merck), followed by (b) a 30-μm layer of photoresist (AZ40XT, Merck). (c) The top layer is patterned using photolithography. (d) An approximately 200-μm thick layer of compliant gel (PDMS CY 52-276, Dowsil) is spin coated on the mold and cured by baking. (e) A glass wafer is bonded to the gel surface using oxygen plasma. (f) Photoresist layers are subsquently dissolved with acetone, after which the surface is immersed in water to rinse and then allowed to dry in ambient conditions; thus, the textured surface is released.

underlying surface texture to further control self-assembly of particles or droplets on surfaces, which may open new avenues for microfabrication techniques. Future study of the dynamic response of solid surfaces to changing outer fluids may also lead to new directions for producing environmentally responsive soft machines, valves, or other tools to be used, for example, in microfluidic devices.

Data and code supporting this study are openly available from Ref. [47].

APPENDIX A: MOLD FABRICATION

To produce the rigid mold, first, we spin-coat and cure two polymeric layers onto a silicon wafer: The first is a sacrificial photoresist layer in contact with the tops of the pillars [Fig. 6(a)] and the second is a photoresist that will be patterned by photolithograpy [Fig. 6(b)], which shapes the pillars' side walls. After exposure and development, the desired pattern of cuboid holes is produced [Fig. 6(c)]. PDMS (Dowsil CY 52-276) is spin-coated into the mold and cured by baking at 80°C for 30 min [Fig. 6(d)]. To support the compliant material, a glass surface is bonded to the PDMS using
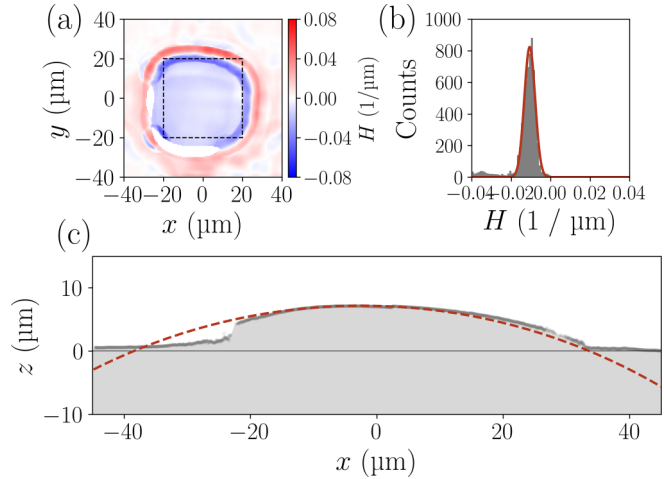

FIG. 7. Pillars deform into approximately spherical caps. (a) Mean curvature field $H(x, y)$ for a compliant micropillar ($G \approx 1$ kPa) with spacing $p = 90$ μm. Negative curvature indicates that the pillar curves toward the $-\hat{z}$ direction. (b) Histogram of H considering data within the box shown in (a). A Gaussian fit (solid line) has peak at $H_{\text{peak}} = -0.010 \pm 0.003$ 1/μm (68% confidence interval). (c) Circular arc (dashed red line) with radius of curvature $\mathcal{R} = 94$ μm superimposed on the pillar profile (gray points).

oxygen plasma [Fig. 6(e)]. Then, by dissolving the mold in acetone, the compliant micropillars are released, after which they are rinsed by immersion in deionized water and dried in air at room temperature [Fig. 6(f)]. This technique can be used to produce 3D pillars [see Figs. 1(d)–1(e)] as well as more complex shapes. Complete fabrication steps, tools, and parameters are provided in detail in Supplemental Material [32].

APPENDIX B: CURVATURE

It can be shown that each deformed pillar has an approximately constant curvature H_0; that is, each pillar deforms into approximately a spherical cap, allowing us to measure well-defined H_0 values that are plotted in Fig. 3. As an example, the curvature field for a pillar at $p = 90$ μm is shown in Fig. 7(a). Curvature across the top of the pillar is negative, indicating that the pillar curves toward the surface. Moreover, H varies little across the pillar center, as demonstrated by the narrow spread in the histogram of H shown in Fig. 7(b), indicating that the initial cuboid has deformed into an approximately spherical cap with radius $\mathcal{R} = 1/|H_0|$, where H_0 is the value of H at the location of the Gaussian peak. The radius of curvature is $\mathcal{R} = 94$ μm and a circular arc with this radius overlaid onto the profile is an excellent match [Fig. 7(c)]. Thus, H_0 is a well-defined measure of curvature for the deformed compliant pillars.

[1] S. Mora, T. Phou, J.-M. Fromental, L. M. Pismen, and Y. Pomeau, Capillarity driven instability of a soft solid, Phys. Rev. Lett. **105**, 214301 (2010).

[2] R. W. Style, A. Jagota, C.-Y. Hui, and E. R. Dufresne, Elastocapillarity: Surface tension and the mechanics of soft solids, Annu. Rev. Condens. Matter Phys. **8**, 99 (2017).

[3] J. Bico, É. Reyssat, B. Roman, Elastocapillarity: When surface tension deforms elastic solids, Annu. Rev. Fluid Mech. **50**, 629 (2018).

[4] B. Andreotti and J. H. Snoeijer, Statics and dynamics of soft wetting, Annu. Rev. Fluid Mech. **52**, 285 (2020).

[5] O. D. Gordan, B. N. J. Persson, C. M. Cesa, D. Mayer, B. Hoffman, S. Dieluweit, and R. Merkel, On pattern transfer in replica molding, Langmuir **24**, 6636 (2008).

[6] D. Paretkar, X. Xu, C.-Y. Hui, and A. Jagota, Flattening of a patterned compliant solid by surface stress, Soft Matter **10**, 4084 (2014).

[7] A. Jagota, D. Paretkar, and A. Ghatak, Surface-tension-induced flattening of a nearly plane elastic solid, Phys. Rev. E **85**, 051602 (2012).

[8] N. Bain, A. Jagota, K. Smith-Mannschott, S. Heyden, R. W. Style, and E. R. Dufresne, Surface tension and the strain-dependent topography of soft solids, Phys. Rev. Lett. **127**, 208001 (2021).

[9] N. Lapinski, Z. Liu, S. Yang, C.-Y. Hui, and A. Jagota, A surface with stress, extensional elasticity, and bending stiffness, Soft Matter **15**, 3817 (2019).

[10] S. Mora, C. Maurini, T. Phou, J.-M. Fromental, B. Audoly, and Y. Pomeau, Solid drops: Large capillary deformations of immersed elastic rods, Phys. Rev. Lett. **111**, 114301 (2013).

[11] C.-Y. Hui, Z. Liu, N. Bain, A. Jagota, E. R. Dufresne, R. W. Style, R. Kiyama, and J. P. Gong, How surface stress transforms rough profiles and adhesion of rough elastic bodies, Proc. R. Soc. A. **476**, 20200477 (2020).

[12] A. Chakrabarti and M. K. Chaudhury, Surface folding-induced attraction and motion of particles in a soft elastic gel: Cooperative effects of surface tension, elasticity, and gravity, Langmuir **29**, 15543 (2013).

[13] A. Chakrabarti and M. K. Chaudhury, Elastocapillary interaction of particles on the surfaces of ultrasoft gels: A novel route to study self-assembly and soft lubrication, Langmuir **30**, 4684 (2014).

[14] S. Karpitschka, A. Pandey, L. A. Lubbers, J. H. Weijs, L. Botto, S. Das, B. Andreotti, and J. H. Snoeijer, Liquid drops attract or repel by the inverted Cheerios effect, Proc. Natl. Acad. Sci. USA **113**, 7403 (2016).

[15] R. Shuttleworth, The surface tension of solids, Proc. Phys. Soc., Sec. A **63**, 444 (1950).

[16] E. R. Jerison, Y. Xu, L. A. Wilen, and E. R. Dufresne, Deformation of an elastic substrate by a three-phase contact line, Phys. Rev. Lett. **106**, 186103 (2011).

[17] A. Chakrabarti, A. Porat, E. Raphaël, T. Salez, and M. K. Chaudhury, Elastowetting of soft hydrogel spheres, Langmuir **34**, 3894 (2018).

[18] H. Liang, Z. Cao, Z. Wang, and A. V. Dobrynin, Surface stress and surface tension in polymeric networks, ACS Macro Lett. **7**, 116 (2018).

[19] X. Shao, J. R. Saylor, and J. B. Bostwick, Extracting the surface tension of soft gels from elastocapillary wave behavior, Soft Matter **14**, 7347 (2018).

[20] R. D. Schulman, M. Trejo, T. Salez, E. Raphaël, and K. Dalnoki-Veress, Surface energy of strained amorphous solids, Nat. Commun. **9**, 982 (2018).

[21] J. D. Berman, M. Randeria, R. W. Style, Q. Xu, J. R. Nichols, A. J. Duncan, M. Loewenberg, E. R. Dufresne, and K. E. Jensen, Singular dynamics in the failure of soft adhesive contacts, Soft Matter **15**, 1327 (2019).

[22] M. Coux and J. M. Kolinski, Surface textures suppress viscoelastic braking on soft substrates, Proc. Natl. Acad. Sci. USA **117**, 32285 (2020).

[23] M. A. J. van Limbeek, M. H. Essink, A. Pandey, J. H. Snoeijer, and S. Karpitschka, Pinning-induced folding-unfolding asymmetry in adhesive creases, Phys. Rev. Lett. **127**, 028001 (2021).

[24] R. J. Donnelly and W. Glaberson, Experiments on the capillary instability of a liquid jet, Proc. Roy. Soc. Lond. A **290**, 1423 (1966).

[25] A. Marchand, J. H. Weijs, J. H. Snoeijer, and B. Andreotti, Why is surface tension a force parallel to the interface? Am. J. Phys. **79**, 999 (2011).

[26] In general, Υ is a tensor, but constant Υ is used in the uniform and isotropic case.

[27] G. Zhuang and J. P. Kutter, Anti-stiction coating of PDMS moulds for rapid microchannel fabrication by double replica moulding, J. Micromech. Microeng. **21**, 105020 (2011).

[28] S.-H. Kim, S. Lee, D. Ahn, J. Y. Park, PDMS double casting method enabled by plasma treatment and alcohol passivation, Sens. Actuat. B: Chem. **293**, 115 (2019).

[29] A. Ansari, R. Trehan, C. Watson, and S. Senyo, Increasing silicone mold longevity: A review of surface modification techniques for PDMS-PDMS double casting, Soft Mater. **19**, 388 (2020).

[30] J. N. Lee, C. Park, and G. M. Whitesides, Solvent compatibility of poly(dimethylsiloxane)-based microfluidic devices, Anal. Chem. **75**, 6544 (2003).

[31] Acetone has been shown to swell PDMS by 6% [30], yet because this is a slight effect, we assume gel deformation is not significantly affected by the solvent, especially since acetone is volatile and does not remain within the gel once it is dry.

[32] See Supplemental Material at http://link.aps.org/supplemental/10.1103/PhysRevE.108.L043001 for details about the measurement of G and Υ, steps in the microfabrication procedure, and the data processing method to measure deformed height h_d and curvature H. It also includes Refs. [33–38].

[33] K. Almdal, J. Dyre, S. Hvidt, and O. Kramer, Towards a phenomenological definition of the term 'gel', Polym. Gels Netw. **1**, 5 (1993).

[34] R. Chasset and P. Thirion, Delayed elasticity of 'pure-gum' rubber vulcanisates, J. Rubber Res. Inst. Malaya **22**, 3 (1969).

[35] S. J. Park, B. M. Weon, J. S. Lee, J. Lee, J. Kim, and J. H. Je, Visualization of asymmetric wetting ridges on soft solids with X-ray microscopy, Nat. Commun. **5**, 4369 (2014).

[36] Ted Pella, Inc., Microscope slide coverslips (2022), https://www.tedpella.com/histo_html/coverslips.aspx.

[37] A. Daerr and A. Mogne, Pendent_Drop: An ImageJ plugin to measure the surface tension from an image of a pendent drop, J. Open Res. Softw. **4**, 3 (2016).

[38] S. van der Walt, J. L. Schönberger, J. Nunez-Iglesias, F. Boulogne, J. D. Warner, N. Yager, E. Gouillart, T. Yu, and the scikit-image contributors, scikit-image: Image processing in Python, PeerJ **2**, e453 (2014).

[39] Mean curvature H is computed by fitting a paraboloid to local subsets of the pillar surface, from which we compute the curvature at each point, as described in detail in Supplemental Material [32].

[40] T. Tanaka, M. Morigami, and N. Atoda, Mechanism of resist pattern collapse during development process, Jpn. J. Appl. Phys. **32**, 6059 (1993).

[41] N. Chakrapani, B. Wei, A. Carrillo, and R. S. Kane, Capillarity-driven assembly of two-dimensional cellular carbon nanotube foams, Proc. Natl. Acad. Sci. USA **101**, 4009 (2004).

[42] D. Chandra and S. Yang, Stability of high-aspect-ratio micropillar arrays against adhesive and capillary forces, Acc. Chem. Res. **43**, 1080 (2010).

[43] S. H. Kang, B. Pokroy, L. Mahadevan, and J. Aizenberg, Control of shape and size of nanopillar assembly by adhesion-mediated elastocapillary interaction, ACS Nano **4**, 6323 (2010).

[44] J. Paulose, D. R. Nelson, and J. Aizenberg, Two-parameter sequential adsorption model applied to microfiber clustering, Soft Matter **6**, 2421 (2010).

[45] Z. Wei, T. M. Schneider, J. Kim, H.-Y. Kim, J. Aizenberg, and L. Mahadevan, Elastocapillary coalescence of plates and pillars, Proc. R. Soc. A. **471**, 20140593 (2015).

[46] G. Zabow, Reflow transfer for conformal three-dimensional microprinting, Science **378**, 894 (2022).

[47] L. Molefe and J. M. Kolinski, dataset for "Elastocapillary menisci mediate interaction of neighboring structures at the surface of a compliant solid", doi:10.5281/zenodo.8307888.